

Evaluation of barrier pillar for seismic hazard reduction at the Kiirunavaara mine

J. Andersson^a, M. Svartsjaern^a, G. Shekhar^b, M. Boskovic^c, E. Swedberg^c, J. Töyrä^c

^a*ITASCA Sweden*

^b*BHP, Australia*

^c*Luossavaara-Kiirunavaara Aktiebolag (LKAB), Sweden*

ABSTRACT

In May 2020, the largest mining-induced seismic event ever recorded in Sweden occurred in the LKAB Kiirunavaara sublevel caving mine. The incident caused significant damage along several hundred meters of drifts. Following the incident, production was paused in the affected area (called Block 22; B22) and two main actions plans for resuming production were developed: (i) leave a temporary residual sill pillar that could be recovered, or left behind, as part of resumed sublevel caving, or (ii) leave a permanent barrier pillar constituting the entirety of B22, effectively dividing the Kiirunavaara Mine into a northern and southern portion. While both actions plans were evaluated from a rock mechanics perspective, the design and evaluation of the latter is the focus of this article. The design and evaluation process for the barrier pillar option was split in two parts. Part 1 considered the quasi-static stability of the barrier pillar and potential seismic indicators as well as the placement of the pillar with respect to minimizing ore losses in B22. A crucial step in this part was to define criteria for stability and thresholds for seismic potential. Part 2 of the evaluation assessed the influence of the barrier pillar on mine infrastructure. In the end, LKAB choose to move forward with the alternative with a barrier pillar of approximately 600 m width extending down to the 1365 m level to be left in the area. The decision was primarily based on the rock mechanics analysis and modeling results presented here.

1 INTRODUCTION

The LKAB Kiirunavaara Mine is a sublevel cave mine in northern Sweden with an annual production of about 27 Mt, with the current deepest extraction point about 1000 m below the ground surface. In May 2020 a seismic event originated in mining Block 22 (B22) causing significant damage to mine infrastructure over a large volume.

Following the event two main action plans were developed to resume caving. The first plan looked at the creation of a temporary sill pillar consisting of the 1022 m and 1051 m mining levels and resuming mining in B22 on the 1079 m level. The sill pillar would then be recovered by controlled caving and the production would fall

in line with the intended global mining sequence (Svartsjaern et al., 2022).

The second option and the focus of this paper outlines the steps taken for the option of leaving a barrier pillar in B22 to reduce the likelihood of further large seismic events in the area. The work was divided into two parts where part 1 focused on establishing stable pillar dimensions and part 2 focused on the influence of the creation and longevity of the pillar with respect to production infrastructure.

2 DETERMINING PILLAR DIMENSIONS

Barrier pillar sizing was aided by numerical analysis using *FLAC3D* (Itasca, 2021). Sizing was performed through the creation of a very large pillar in the study area (B15–B26) in the

model, and then complete sequential excavation of the orebody on both sides of the pillar region. The pillar horizontal extent was then reduced in steps and the pillar response was monitored.

2.1 Geology and pillar definition

A geological model consisting of the orebody, two diabase dykes (DB), porphyry rock (syenite-porphyry–SP, diabase porphyry–DP, and quartz-porphyry–QP) as well as a definition of the boundary between the footwall and hangingwall host rock, see Figure 1, was used as base for the analysis. Included in the model was also a zone of crushed rock with low RQD.

To define the region that would form the initial pillar, a block model of the orebody was created. A series of cubic blocks with 14.25 m side length was first created between the mine coordinates $Y=2800$ and $Y=1600$. The block size was chosen as being approximately half the average height between the mining levels in B22. Following this step, blocks that were located inside the orebody or intersecting its boundary were kept while the rest of the blocks were removed. In certain areas blocks that were intersecting the rock types of SP, QP, DP or DB were also kept, avoiding leaving holes in the pillar that could potentially act as stress concentrators. The final remaining blocks were then used to group the zones in the main *FLAC3D* model forming the maximum extents of the initial barrier pillar, see Figure 2.

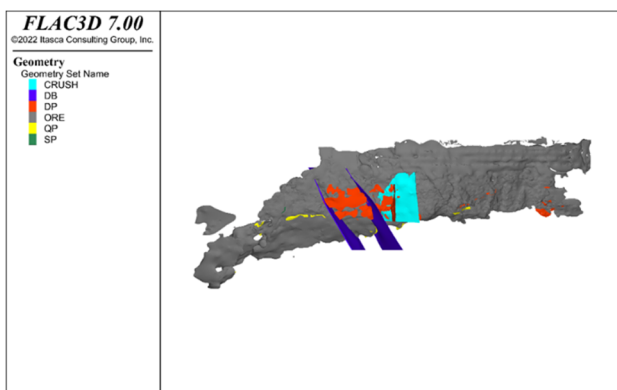


Figure 1 Geological entities together with the crushed zone.

Mined areas were left as open voids in the model. This equates to a conservative pillar stability analysis because in the true case the caved

rock would provide some confinement and support to the abutments of the pillar.

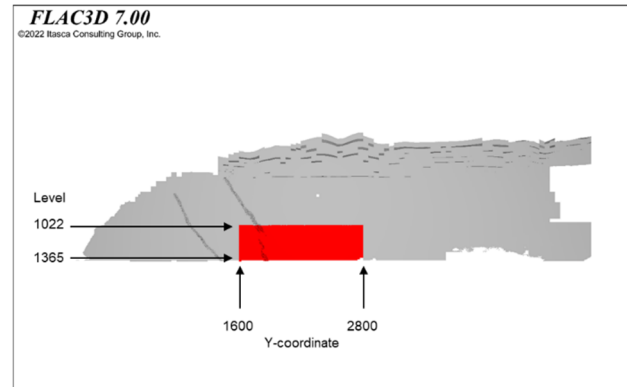


Figure 2 Mined areas (gray) together with the pillar.

2.2 Numerical pillar reduction

The pillar was sequentially reduced by the removal of individual vertical slices. The slicing for an individual step could be performed on either the north or south pillar boundary, but not both simultaneously. The pillar height was kept constant between the 1022 and 1365 m levels, see Figure 3. Before a slice of the pillar was extracted the volume of ore in each of the two outer slices was calculated, the slice with the largest volume of ore was then excavated. This process was repeated until the pillar was completely excavated.

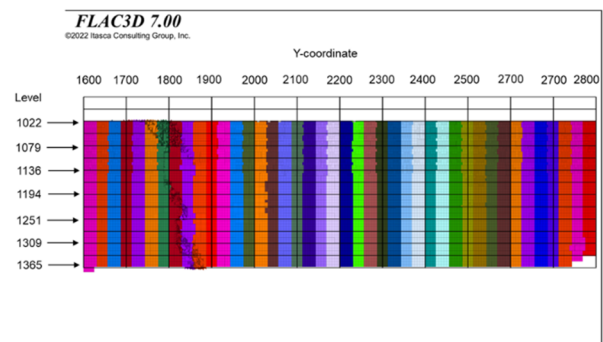


Figure 3 Initial pillar and the different slices.

2.3 Material properties

The numerical model used the Itasca developed constitutive model *IMASS* (*Itasca Constitutive Model for Advance Strain Softening*, Ghazvinian et al., 2020). A sensitivity analysis was performed in which the influence of changes in the

material properties on pillar final extent were investigated using three sets of material properties.

1. The base case consisted of average rock mass parameter according to Table 1.
2. Alternative case 1 used lower bound rock mass parameters according to Table 2 to analyze the sensitivity to rock mass quality being systematically overestimated.
3. Alternative case 2 was used to analyze the sensitivity to local rock mass deterioration in the pillar volume from e.g., the 2020 seismic event or hydrofracturing (preconditioning) conducted in the area. For this case material properties in Table 3 were used for rock types located outside the pillar while properties from Table 4 were used for rock types located inside the pillar.

Rock volumes located inside the crushed zone had their baseline *GSI* reduced by 10 in all models. Note that the hangingwall was modelled as "fake elastic" by preventing hangingwall yielding by setting the *UCS* to extremely high values. This step was required to prevent excessive hangingwall yield and displacement due to the mined volumes being simulated as voids.

Table 1 *IMASS* rock mass parameters for the base case

Geology	<i>UCSi</i> (MPa)	<i>mi</i>	<i>Ei</i> (GPa)	<i>GSI</i>	ρ (kg/m ³)
FW	180	20	65	76	2700
HW	12600	18	65	61	2700
Ore	183	17	60	67	4600
DB	175	15	65	44	2700
QP/SP /DP	320	20	65	81	2700

Table 2 *IMASS* rock mass parameters for case 2

Geology	<i>UCSi</i> (MPa)	<i>mi</i>	<i>Ei</i> (GPa)	<i>GSI</i>	ρ (kg/m ³)
FW	180	20	60	58	2700
HW	12600	20	60	50	2700
Ore	180	20	60	58	4600
DB	100	15	60	40	2700
QP/SP /DP	320	20	60	70	2700

Table 3 *IMASS* rock mass parameters for geology outside the pillar in case 3

Geology	<i>UCSi</i> (MPa)	<i>mi</i>	<i>Ei</i> (GPa)	<i>GSI</i>	ρ (kg/m ³)
FW	180	20	65	76	2700
HW	12600	18	65	66	2700
Ore	180	20	60	58	4600
DB	175	15	65	44	2700
QP/SP /DP	320	20	65	81	2700

Table 4 *IMASS* rock mass parameters for geology inside the pillar in case 3

Geology	<i>UCSi</i> (MPa)	<i>mi</i>	<i>Ei</i> (GPa)	<i>GSI</i>	ρ (kg/m ³)
FW	180	20	60	58	2700
HW	180	18	60	51	2700
Ore	180	20	60	58	2700
DB	100	15	60	40	4600
QP/SP /DP	320	20	60	70	2700

2.4 Pillar reduction response

The evaluation of pillar widths was done in two parts based on quasi-static stability and quasi-static seismic indicators.

Quasi-static stability was evaluated based on the stress magnitude, calculated strength-factor (*SSR*) and material yielding state for the different reduction steps.

SSR is calculated as a local indicator of the current stress state's proximity to failure. With the current effective minimum and maximum principal stresses denoted as σ_1 and σ_3 , the current Mohr circle can be plotted as in Figure 4. By keeping σ_3 fixed, the Mohr circle is enlarged so that it is tangent to the shear failure line; the new minimum effective principal stress is denoted by σ'_1 , and the strength-stress ratio is defined as equation 1.

$$SSR = \left| \frac{\sigma'_1 - \sigma_3}{\sigma_1 - \sigma_3} \right| \leq 10 \quad (1)$$

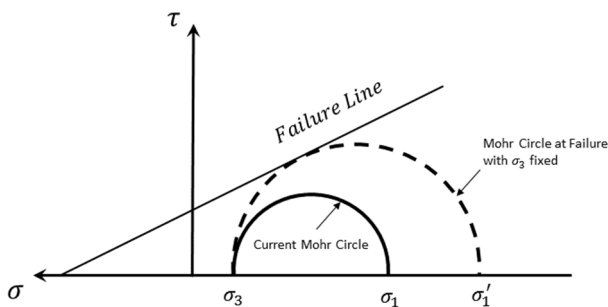


Figure 4 Schematic of strength-stress ratio.

Material yielding state indicates whether the material is in an elastic state or if it is in a plastic state. Plastic yielding will result in the stresses causing yielding to be redistributed and the material may then again behave elastically but have been permanently altered e.g., through new fracture formation.

Both the major principal stress (σ_1) and *SSR* were calculated along lines in the central location of the pillar (with respect to height and width). These evaluation lines followed along the central point in each slice of the pillar via a plane placed in the middle of the pillar lateral extent. Values were evaluated both as point-per-point and as an average value for all the zones

that were located inside the pillar. The average value was calculated by summing up the value from each zone and then dividing the sum by the number of zones in the summation.

For the average of the major principal stress in the pillar there was a gradual increase in the average stress until a pillar width of around 290 m, where it reached a plateau. This plateau then continued until the pillar reached a width of 230 m. At 210 m it was apparent that the trend was changing, the pillar started to unload/shed stresses as indicated by a decrease in the average stress in the pillar, see Figure 5.

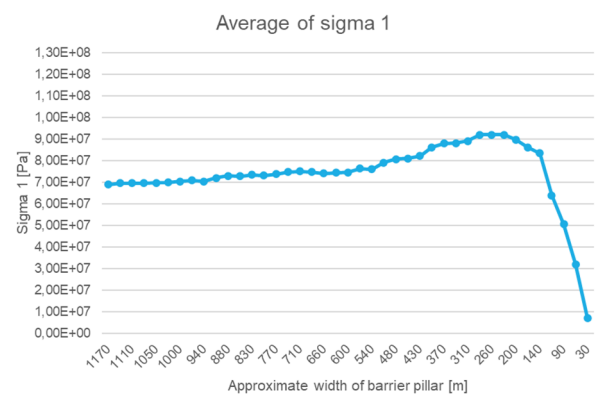


Figure 5 Average of sigma1 in the pillar.

The average of *SSR* in the pillar (calculated in the same way as the average of the major principal stress) is shown in Figure 6. A change in trend was noted starting at a width around 340 m where the *SSR* begins to decrease faster than for previous widths. At a width of 110 m the *SSR* increased again, caused by most of the pillar being yielded and the stresses being redistributed elsewhere.

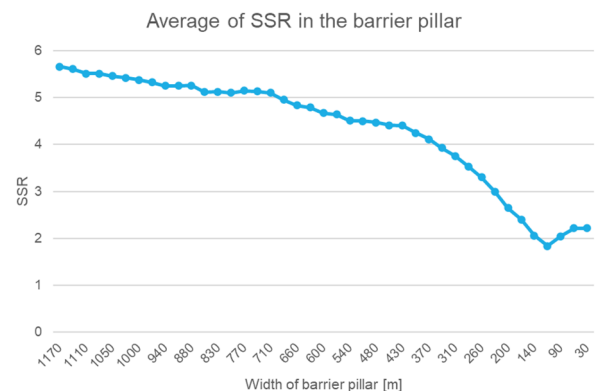


Figure 6 Average of SSR in the pillar.

For pillar widths down to 290 m the stress line forms a U-shape indicating that the pillar abutments are still able to take the increase in stresses from reducing the pillar. When the pillar was narrowed down with another slice to 260 m the southern abutment of the pillar started to fail, which is indicated by a lowering of stress magnitude and a loss of the U shape in the chart, see Figure 7. Results shows that even though the abutment started to fail, the pillar core was capable of carrying additional loads down to a width of 140 m, whereafter also the center area starts to shed stresses, see Figure 8.

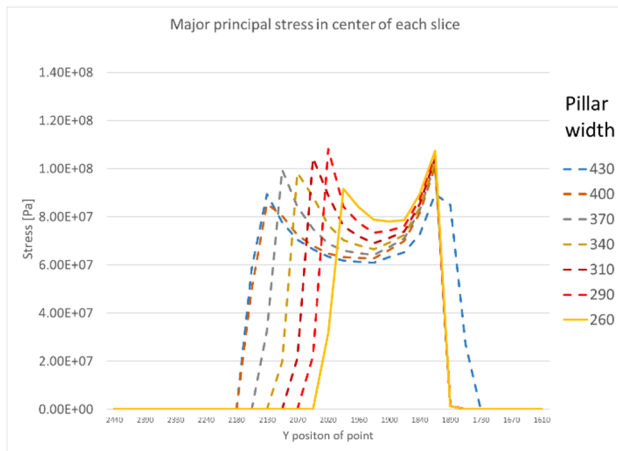


Figure 7 Major principal stress in the center of each slice.

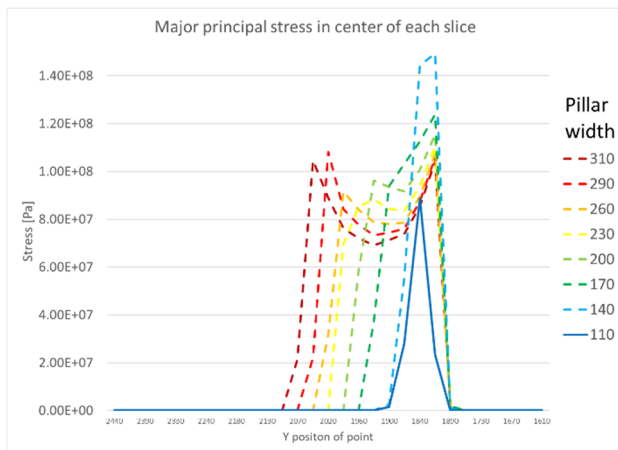


Figure 8 Major principal stress in the center of each slice.

Evaluation of yielding was performed in a plane placed in the approximated center of the pillar and using a "rule of thumb" that a pillar could be considered stable if 1/3 of the pillar center remains unyielded.

Pillar reduction indicated that more than 1/3 of the pillar remains unyielded for pillar widths down to 170 m. When the width of the pillar was reduced further, down to 140 m, the increase in accumulated yielding was enough to bring the pillar close to the 1/3 ratio and for smaller widths it did surpass the 1/3 ratio, see Figure 9 and Figure 10.

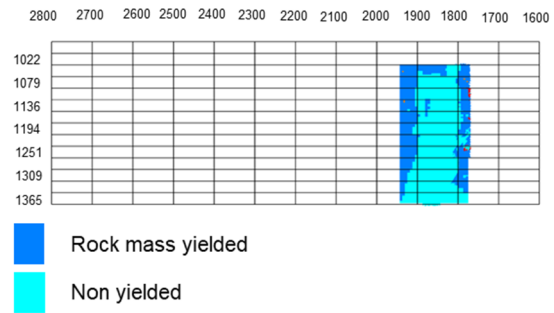


Figure 9 Yielding in pillar center for a 170m pillar.

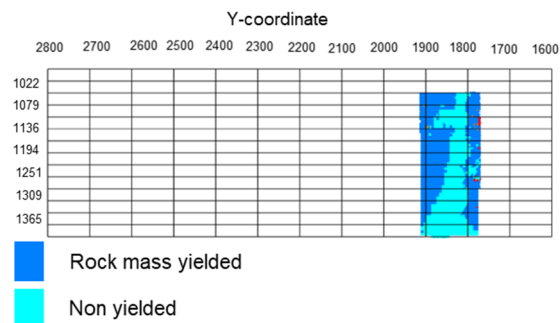


Figure 10 Yielding in pillar center for a 140m pillar.

Following the analysis of static stability, quasi-static seismic indicators were used to indicate pillar widths with disproportional seismic potential. The proportionality of seismic response was evaluated based on changes in pillar stress behavior at specific magnitude ranges. The magnitude ranges were based on earlier work where damage mapping in the mine was performed and a numerical model was used to estimate stress levels at the time and place of the damage.

Stress values were gathered from the stress evaluation lines in the pillar center. For the major principal stress (σ_1) the threshold value was set to 55 MPa which corresponds to the value in which 80 % of stress-induced failures are ex-

pected to occur at or below, see Figure 11 based on the work by Perman *et al.* (2021).

The threshold value for tangential stress (σ_t) (calculated according to Equation 2), which can be seen as an approximation of stress around an excavation boundary, was set to 130–150 MPa. This range corresponds to the value for the tangential stress in which 50–80 % of the stress induced failures are expected to occur at or below, see, Figure 12. This also corresponds to 60–70% of pillar UCS and the upper part of fracture initiation threshold. Tangential stress was used to estimate the potential for stope-near seismicity (events located close to the excavation boundary).

$$\sigma_t = 3 * \sigma_1 - \sigma_3 \quad (2)$$

The threshold value for differential stress (σ_D) (calculated according to Equation 3) in the northern parts where diabase dyke is located was set to 90 MPa. This corresponds to 40–50% of the pillar UCS and the lower part of fracture initiation threshold. Differential stress was used to estimate the potential of far-field seismicity i.e., events located in the rock mass outside the direct influence area of individual infrastructure sets.

$$\sigma_D = \sigma_1 - \sigma_3 \quad (3)$$

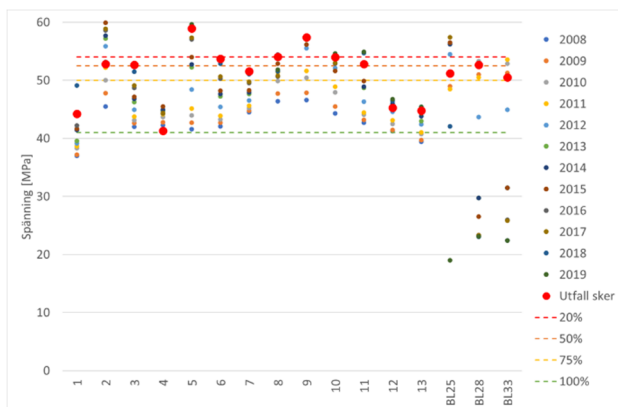


Figure 11 Value of the major principal stress at the point of stress induced failure.

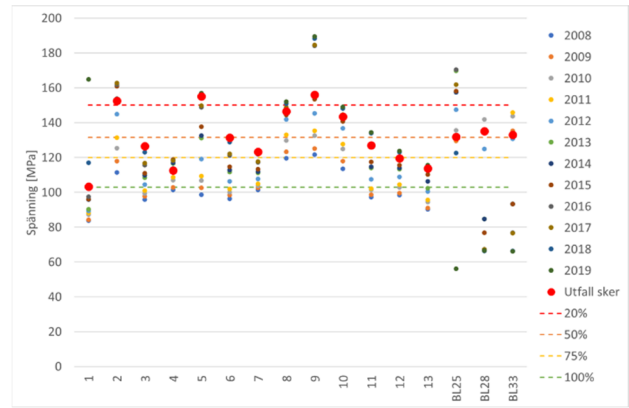


Figure 12 Value of the tangential stress at the point of stress induced failure.

For the major principal stress, the threshold, 55 MPa, was reached for 600 m wide pillar. At this point a U-shape was still maintained along the stress evaluation line, see Figure 13. Further reduction of the pillar width causes the bottom of the U-shape (pillar center) to lift above the 55 MPa threshold. The same behavior, a change in trend for the pillar center (within the set threshold range), was evident for a 600 m wide pillar for both the major principal and tangential stress, Figure 15. For the same pillar dimension, a sharp rise could be noted at the northern abutment of the pillar compared to previous mining steps, see Figure 15, indicating a potential increase of seismic response close to the southern diabase dyke.

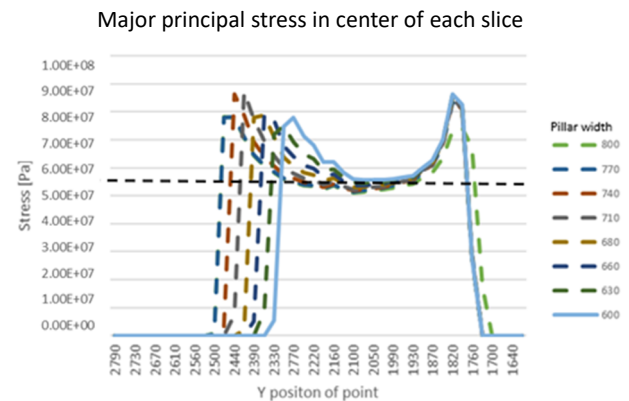


Figure 13 Major principal stress in the center of each slice.

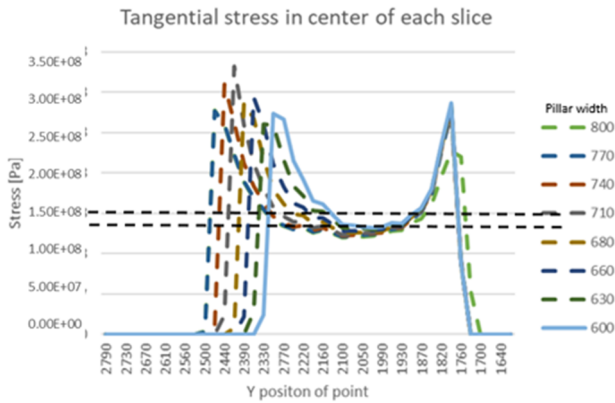


Figure 14 Tangential stress in the center of each slice.

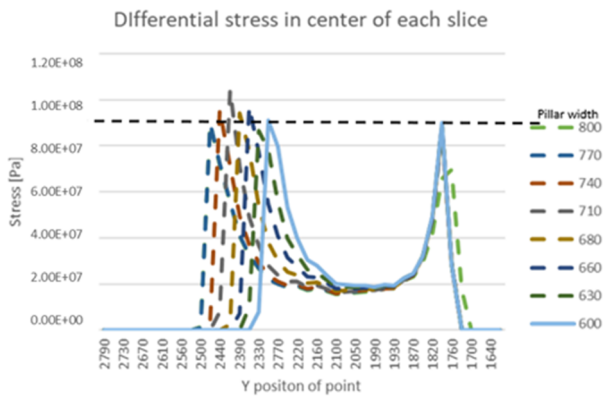


Figure 15 Differential stress in the center of each slice.

2.5 Pillar sizing results

The results and the evaluation criteria for both quasi-static stability and quasi-static seismic indicators were discussed at a workshop held with the mine. It was decided to go forward with a barrier pillar width of 600 m based on the evaluation of seismic potential. A decision was also made to include pillar widths of 500, 600, and 700 m for reference. The pillars were analyzed for placement between the following approximate Y-coordinates:

- 500 m = Y1745 to Y2245
- 600 m = Y1745 to Y2345
- 700 m = Y1745 to Y2445

2.6 Sensitivity analysis

A sensitivity analysis was performed based on the 600 m wide pillar. Two additional cases were evaluated in comparison to the base case. The analysis concluded that case 2 (generally lower rock mass quality) tended to lead to an increase

in the major principal and tangential stress for the central part of the pillar when compared to the base case. However, a notable decrease in the magnitude for the differential stress in the northern part of the pillar could also be observed. Case 3 (damage in pillar area) did instead result in stress magnitudes that were very similar to the base case, see Figure 16 and Figure 17.

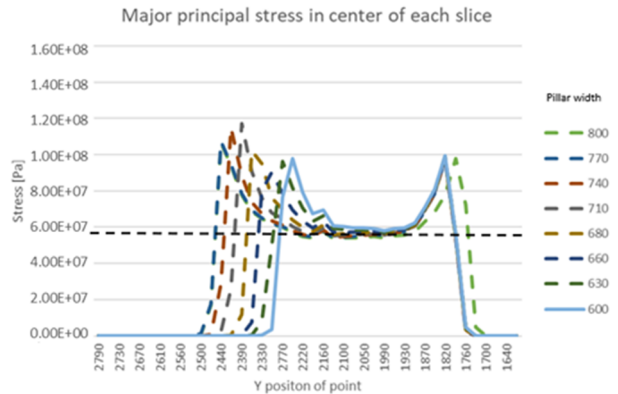


Figure 16 Major principal stress in the center of each slice for case 2.

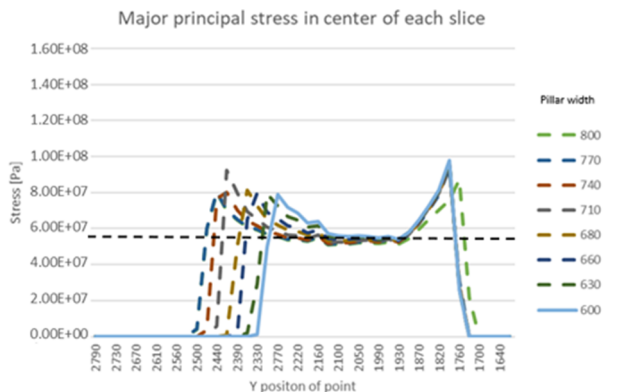


Figure 17 Major principal stress in the center of each slice for case 3.

3 PILLAR INFLUENCE ON INFRA-STRUCTURE

3.1 Method of analysis

For analyzing pillar influence on mining infrastructure code coupling between *FLAC3D* and *CAVESIM* (Sharrock, 2021.) was used to model realistic caving progression from the 2019 mining front down to level 1365 m. SLC mining was simulated on a ring-by-ring basis with a data transfer window between the codes (length between periods) equivalent to 1 year of production.

3.2 Geological model and material properties

The *FLAC3D* model for this analysis used the same geological entities that was described in part 1 (pillar sizing) with the addition of some large-scale structures in the hangingwall that were not included in part 1. The catalogue of large-scale structures is based on the work by Mattsson (2017). From this catalogue a number of structures were judged to be geologically distinctive enough to be included in the *FLAC3D* model. The relative locations of the structures included are shown in Figure 18. Mining of planned production in the model started from the year 2019, the cave shape created from earlier mining was imported from earlier cave modeling for the mine and used to define areas of caved rock at the start of the simulation, see Figure 19.

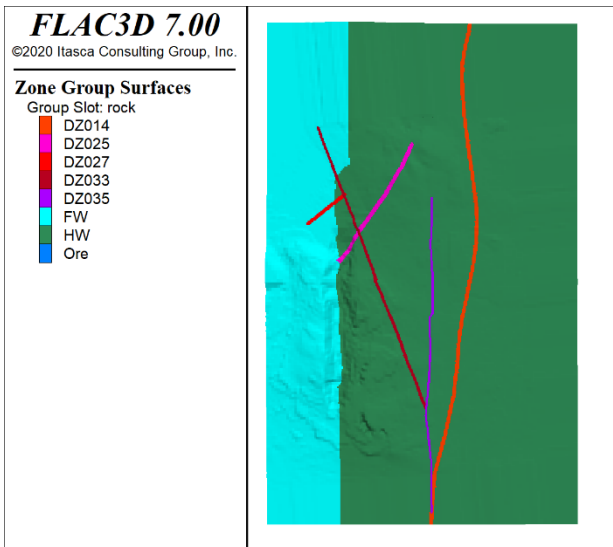


Figure 18 Large-scale structures adapted from the Mattsson (2017) catalogue with additions of DZ025 and DZ027 (U.-B. Andersson, personal communication, dec 04, 2018).

Compared to the sizing model a change was made for the properties in the hangingwall as the hangingwall was no longer required to be modeled as a "fake elastic" material due to the introduction of explicit cave material in the SLC. Properties used for the hangingwall as well as properties for the DZ structures are shown in Table 5. The remaining geological entities used properties from Table 1. The *GSI* was reduced by

10 compared to the rock type base line values for volumes located inside the crushed zone.

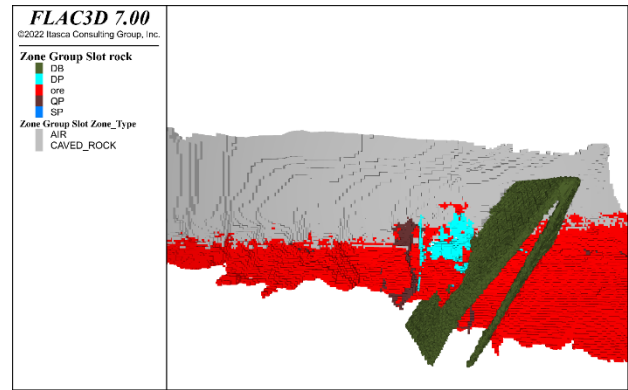


Figure 19 Geological entities and caved rock seen from the hangingwall towards the footwall (DZ structures hidden for visual clarity).

Caved rock was modelled as a frictional Mohr-Coulomb material with a Young's modulus of 0.2 GPa and an internal friction angle of 43° based on experience from Australian caving mines.

Table 5 Additional parameters for Part 2.

Geology	$UCSi$ (MPa)	m_i	E_i (GPa)	GSI	ρ (kg/m ³)
DZ-structures	180	20	65	20	2700
HW	150	18	65	66	2700

3.3 Zero-option base case

In order to evaluate the influence of a pillar in B22, a comparison was made with a theoretical (but unachievable) zero-case where mining was carried on as usual with no pillar left behind. However, due to time restraints, no model without a pillar was created for this project. Instead, a comparison was made with results retrieved from a model created for a different, parallel, project. The no-pillar model (zero-option case) was a global mining sequence model created for another *LKAB* project and, even though similar to the pillar models used in this project, there are some differences that must be highlighted.

The main difference is that the zero-case model uses a different set of material properties which were scaled to mine scale behavior and were thus in general lower than the block scale parameters used for the barrier pillar analysis. The geology was also less detailed, particularly in B22 for the zero-case model (no porphyry intrusions) also leading to some minor differences in the orebody definition, see Figure 20 and Figure 21. The zero-case model also did not include the diabase.

With these differences in mind, and under the circumstance that the comparisons are made focusing on the trends of the stresses between the models rather than the magnitude of stress, the comparison is viable as an indicator for pillar influence on the global stress state. In order to make this comparison more viable, an effort was made to retrieve stress values from volumes that were non-yielded in both models and thus minimize the dependence of differing rock properties between the models.

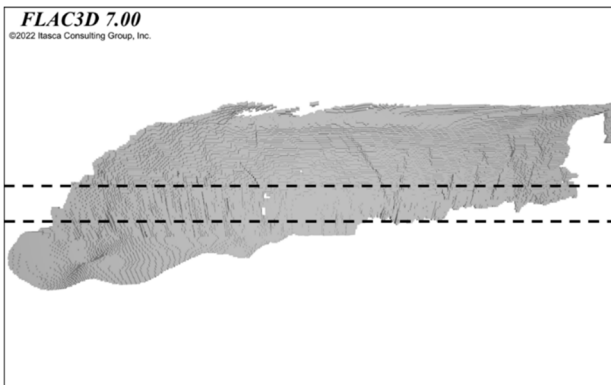


Figure 20 Shape of the orebody in the zero-case model, dashed lines indicate levels 1079 and 1365 m. Model seen from footwall side.

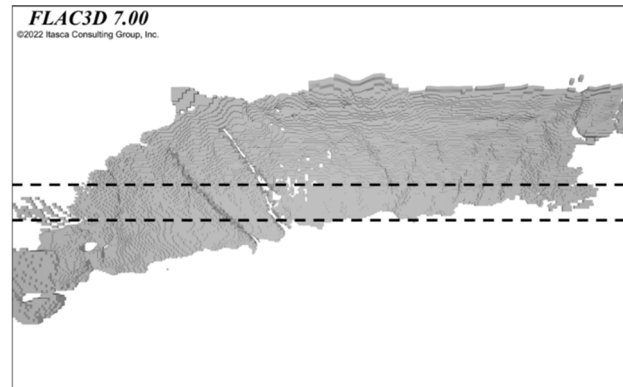


Figure 21 Shape of the orebody in the pillar model, dashed lines indicate levels 1079 and 1365 m. Model seen from footwall side.

3.4 Influence on stresses along footwall drifts.

Differential and tangential stresses were compared between the different models in points along footwall drift locations with a spacing of 50 m between each point. However, since no infrastructure was explicitly included in the models the location of the drifts was approximated to be located along a line 20 m into the footwall from the ore-footwall contact. Stresses from each level were taken at the mining period before the plow in the production (deepest mining level in the mine) reaches the evaluated level, i.e., stresses are retrieved for a footwall drift one level below the deepest point of production at any given time. The stresses were collected from non-yielded areas for virtually all surveyed points.

The results show that for footwall drifts above the 1194 m level the models with and without a pillar resulted in similar stress trends i.e., the width of the pillar did not influence the result in any notable way. Examples of this can be seen in Figure 22 showing results for the 1137 m level.

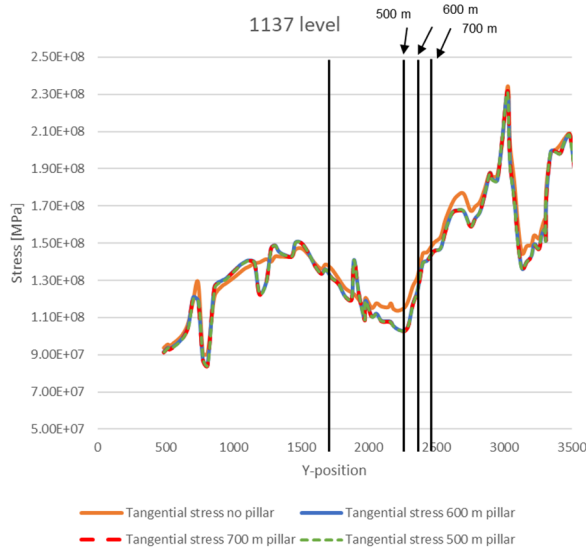


Figure 22 Tangential stresses along the footwall drift at the 1137 m level.

For footwall drifts located at the 1225 m level or deeper the stress trends showed a potential benefit gained with the placement of the pillar. For the portions of the drifts that are located behind the pillar there is a significant potential decrease in both tangential and differential stress for all three pillar cases compared to the no-pillar case. While the portion of footwall drifts that are behind the pillar itself would never be mined in the case of a pillar, the stress reduction is also notable at the pillar abutments at the edges of B15 and B26. The beneficial reduction is most prominent at the northern abutment i.e., at the border of B15.

The reduction results are similar for the three examined pillar dimensions for areas located north of $Y=2000$ (rough pillar center). South of $Y=2000$ there are some differences in the stress curves between the three pillar cases, which is caused by differences in the location of the southern pillar abutment, see Figure 23 through Figure 24 for results from the 1225 and 1338 m levels, respectively.

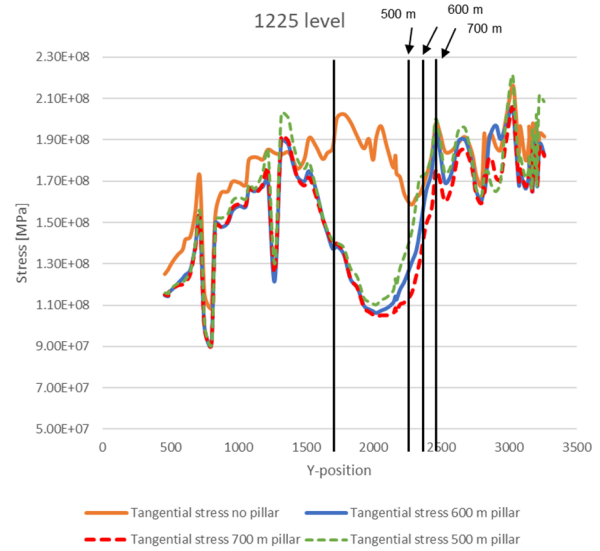


Figure 23 Tangential stresses along the footwall drift at the 1225 m level.

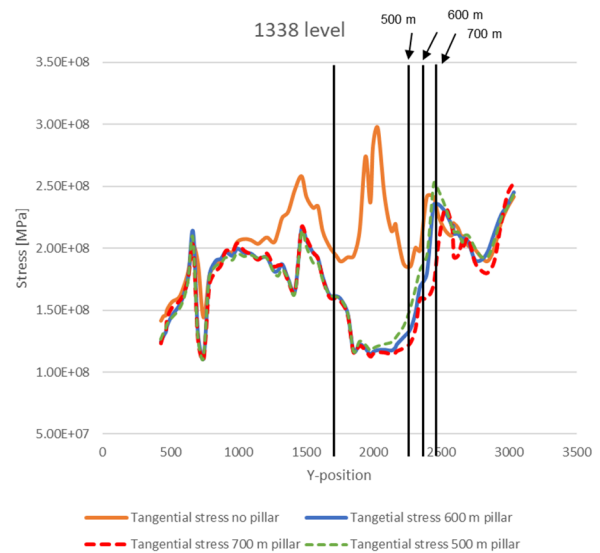


Figure 24 Tangential stresses along the footwall drift at the 1338 m level.

3.5 Influence on stresses along critical infrastructure.

Differential and tangential stresses were evaluated along the locations of the media drifts located on 1165, 1252, and 1338 m levels as well as the 1365 m haulage level and the explicit level 1108 m footwall drift location.

In the graphs for each level, results from when mining was performed above that level are shown as solid lines while dashed lines indicate that the mining at the period was performed at, or below, that level. This means that for e.g., level 1252 m mining between 1108 m and

1225 m are shown as solid lines and mining of 1252–1365 m are shown as dashed lines. Results from the zero-option case model is also included shown as dotted lines in the charts, these dotted lines show results from when mining was performed one level above, at, and one level below the evaluated level.

For infrastructure at the 1108 m level, the stress trends show an increase in stress magnitude for cases that has a pillar compared to the zero-option case. In the pillar models, a large spike in stress magnitudes around Y=1800 can be noted, which cannot be seen in the zero-option model. This is caused by the diabase dyke which was

included in the pillar models but not in the zero-option model and the spike should thus not be included in the comparison, for any of the levels.

When mining continues to deeper levels the stresses in areas located behind the pillar increases, while the stress decreases for areas located either to the north or south of the pillar. The only noticeable differences between the different studied pillar widths was the location at which the stress starts to increase at the southern abutment where a wider pillar has the location moved further to the south, see **Error! Reference source not found.** to **Error! Reference source not found.**

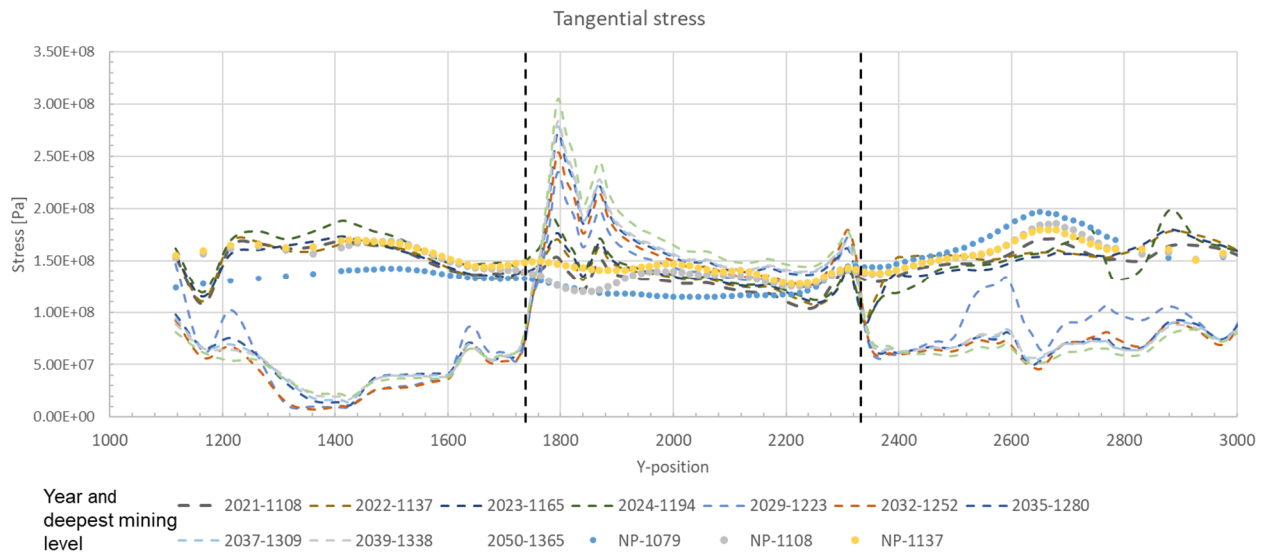


Figure 25 Tangential stress along the 1108 m level for a 600 m wide pillar.

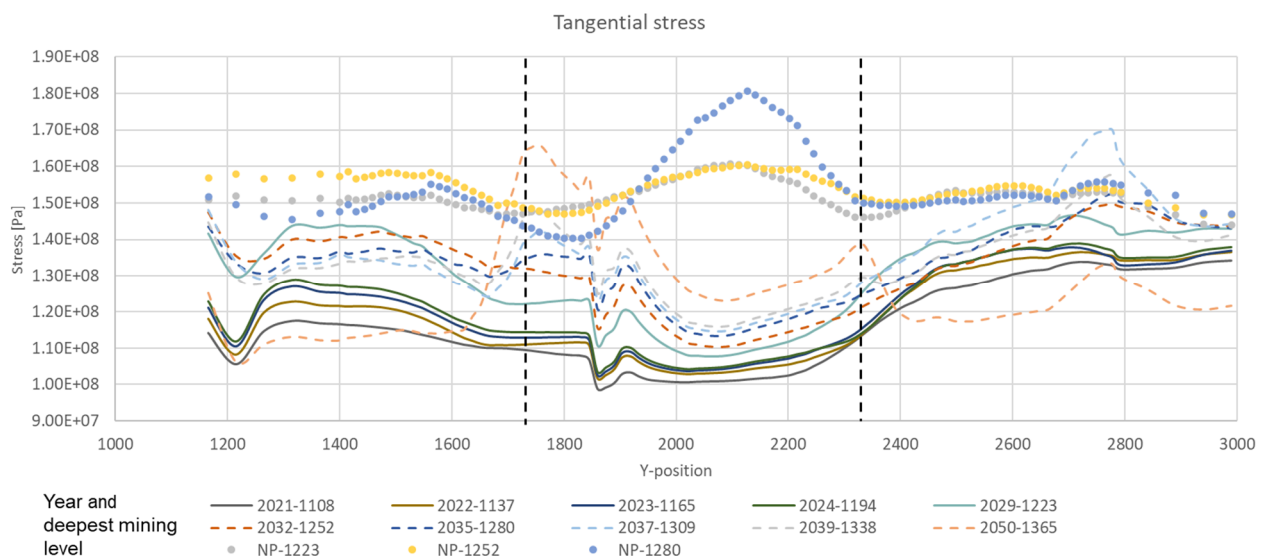


Figure 26 Tangential stress along the 1252 m level for a 600 m wide pillar.

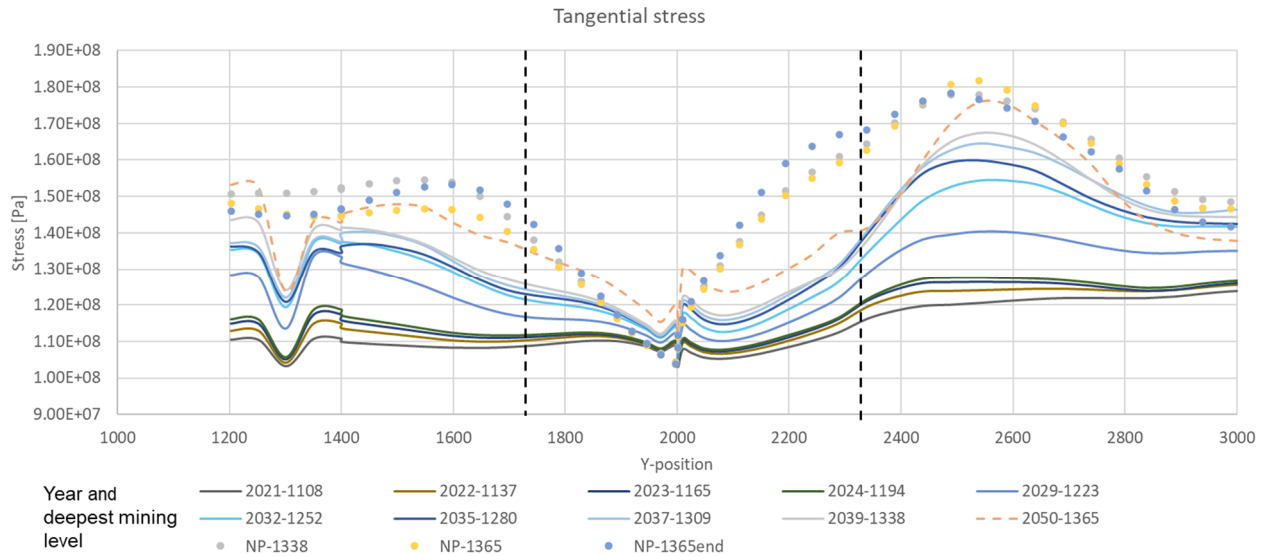


Figure 27 Tangential stress along the 1365 m level for a 600 m wide pillar.

4 DISCUSSION

In part 1 the pillar dimensions were initially evaluated considering two different sets of criteria. The first criteria set evaluated a pillar width that would be stable during quasi-static conditions where the risk of seismic events were not considered. For this case, a stable pillar would end up being around 300 m wide. However, it is clear from the 2020 May event that seismic risk must be considered for the pillar dimension. The uneven mining front of 2020, in effect constituting in a 400 m wide barrier pillar, is suspected to be major driver for the 2020 event. This, in itself, is an indication that a "viable" pillar must have dimensions larger than 400 m in width.

The second set of criteria considered quasi-static seismic indicators (major principal stress, estimated tangential stress and differential stress). This analysis focused on finding a pillar width as small as possible without disproportionately increasing the risk of seismic events inside or adjacent to the pillar. The basis for determining the onset point of disproportional increase in seismic response was a notable change in pillar behavior with respect to the evaluated stress components within a magnitude span known to be associated with rock and infrastructure damage. However, no explicit dynamic response was modelled. The May 2020 event is suspected to be significantly affected by dynamic components taking on a domino-type failure sequence.

The initial 2020 event was likely not the main event, but caused a cascade effect in which nearby, highly loaded areas were triggered by the released energy from the first event resulting in the major combined event. This type of dynamic energy driven failure cannot be summarized from the current models.

For the quasi-static seismic potential evaluation average levels of major principal stress was calculated based on the single stress component only for each zone, i.e., not using a full tensor summation approach. This simplification is not deemed to significantly affect the outcomes of the analysis because the individual stress components were not studied in context of the full stress field. Hence, the evaluation of major principal stress (σ_1) results were not influenced by the relative magnitude of intermediate principal stress (σ_2) and minimum principal stress (σ_3).

Pillar dimensions and pillar influence on adjacent mining infrastructure have been analyzed based on a flat production front meaning more or less equal mining depth on both side of the pillar. The results of this study are valid as long as this assumption holds; based on the suggested final pillar geometry, a level difference on the north relative south sides of the pillar of up to three sublevels is in this context considered to be flat.

5 CONCLUSIONS

- The analysis performed indicate a minimum pillar width of 600 m considering both quasi-static stability and seismic indicators.
- A sensitivity analysis was performed on the minimum pillar. Based on the sensitivity analysis an overall reduction in rock mass properties resulted in the need of a 100 m wider pillar compared to the base case if all parameters were systematically underestimated.
- The effect on existing and planned production (footwall drifts) and long-term infrastructure (media levels and haulage level) were studied. The results indicate that a pillar could have a positive influence on deeper seated mining levels.
- From the 1225 m level and deeper, a significant reduction in stress magnitude could be observed for areas located behind the pillar compared to as if no pillar were there.
- An established barrier pillar has a negative influence on long-term infrastructure (media levels) down to level 1165 m where the models show an increase in stress magnitude behind the pillar compared to the no-pillar case.
- Based on the analysis of footwall drifts and long-term infrastructure the positive aspects from a barrier pillar will not come into effect until the pillar has been fully established
- The establishment of a pillar (mining down to level 1194 m) is not associated with negative effects with the exception of media level 1165 m which will be located inside the stress arch going through the upper boundary of the pillar.
- The choice of pillar widths (500–700 m) has negligible influence on stress magnitudes at infrastructure locations outside the pillar.

- This project has derived minimum pillar dimension for a barrier pillar at B22. The project has also investigated how the establishment and continued existence of such a pillar could affect long-term and active production infrastructure in B15, B22, and B26. Optimization and detailed design of the pillar, including production sequencing and dependencies between the northern and southern sides of the pillar remains and lays outside the scope of this study.
- The effects of a barrier pillar in B22 on the ground surface displacements and caving pattern has not been specifically addressed in this study nor has explicit dynamic failure mechanisms been considered.

ACKNOWLEDGEMENT

The authors greatly acknowledge LKAB for permission to publish the result of this project.

REFERENCES

- Ghazvinian, E., Garza-Cruz, T., Bouzeran, L., Fuenzalida, M., Cheng, Z., Cancino, C. & Pierce, M. (2020). Theory and Implementation of the Itasca Constitutive Model for Advanced Strain Softening (IMASS). In Proceedings of eight international conference & exhibition on mass mining (MASSMIN 2020), R Castro, F Báez, K, Suzuki (eds.). pp 451–461.
- Itasca (2021). *FLAC3D* (Fast Lagrangian Analysis of Continua 3D), Version 7.0. Minneapolis: Itasca Consulting Group, Inc.
- Sharrock, G. (2021). *CAVESIM User's manual*, Version 6.5. Itasca Australia Pty Ltd, Australia
- Svartsjaern, M., Rentzelos, T., Shekhar, G., Swedberg, E., Boskovic, M. & Hebert, Y. (2022). Controlled reopening of the Kiirunavaara production block 22 after a 4.2 magnitude event. In Y Potvin (ed.), *Caving 2022: Proceedings of the Fifth International Conference on Block and Sublevel Caving*, Australian Centre for Geomechanics, Perth, pp. 685–698.
- Svartsjaern, M. (2022). Evaluation of alternative sequences for continued mining in B22 following the May 2020 seismic event. Itasca report to LKAB 2022-05-02.